Author's personal copy

J Biol Inorg Chem (2013) 18:1005–1017
DOI 10.1007/s00775-013-1049-6

ORIGINAL PAPER

Selectivity of Ni(II) and Zn(II) binding to *Sporosarcina pasteurii* UreE, a metallochaperone in the urease assembly: a calorimetric and crystallographic study

Barbara Zambelli · Katarzyna Banaszak · Anna Merloni · Agnieszka Kiliszek · Wojciech Rypniewski · Stefano Ciurli

Received: 11 July 2013 / Accepted: 13 September 2013 / Published online: 15 October 2013
© SBIC 2013

Abstract Urease is a nickel-dependent enzyme that plays a critical role in the biogeochemical nitrogen cycle by catalyzing the hydrolysis of urea to ammonia and carbamate. This enzyme, initially synthesized in the apo form, needs to be activated by incorporation of two nickel ions into the active site, a process driven by the dimeric metallochaperone UreE. Previous studies reported that this protein can bind different metal ions in vitro, beside the cognate Ni(II). This study explores the metal selectivity and affinity of UreE from *Sporosarcina pasteurii* (*Sp*, formerly known as *Bacillus pasteurii*) for cognate [Ni(II)] and noncognate [Zn(II)] metal ions. In particular, the thermodynamic parameters of *Sp*UreE Ni(II) and Zn(II) binding have been determined using isothermal titration calorimetry. These experiments show that two Ni(II) ions bind to the protein dimer with positive cooperativity. The high-affinity site involves the conserved solvent-exposed His^{100} and the C-terminal His^{145}, whereas the low-affinity site comprises also the C-terminal His^{147}. Zn(II) binding to the protein, occurring in the same protein regions and with similar affinity as compared to Ni(II), causes metal-driven dimerization of the protein dimer. The crystal structure of the protein obtained in the presence of equimolar amounts of both metal ions indicates that the high-affinity metal binding site binds Ni(II) preferentially over Zn(II). The ability of the protein to select Ni(II) over Zn(II) was confirmed by competition experiments in solution as well as by analysis of X-ray anomalous dispersion data. Overall, the thermodynamics and structural parameters that modulate the metal ion specificity of the different binding sites on the protein surface of *Sp*UreE have been established.

Keywords UreE · Nickel · *Sporosarcina pasteurii* · Calorimetry · Zinc

B. Zambelli, K. Banaszak, and A. Merloni contributed equally to this work.

An interactive 3D complement page in Proteopedia is available at http://proteopedia.org/w/Journal:JBIC:23.

Electronic supplementary material The online version of this article (doi:10.1007/s00775-013-1049-6) contains supplementary material, which is available to authorized users.

B. Zambelli · A. Merloni · S. Ciurli (✉)
Laboratory of Bioinorganic Chemistry,
Department of Pharmacy and Biotechnology,
University of Bologna, Bologna, Italy
e-mail: stefano.ciurli@unibo.it

K. Banaszak · A. Kiliszek · W. Rypniewski
Institute of Bioorganic Chemistry,
Polish Academy of Sciences, Poznan, Poland

Introduction

Urease [1, 2] is a nickel-dependent enzyme that plays a critical role in the biogeochemical nitrogen cycle by catalyzing the hydrolysis of urea to ammonia and carbamate with a 3×10^{15} fold rate enhancement as compared to the uncatalyzed reaction [3]. The active site of the enzyme contains two Ni(II) ions that are bridged by a posttranslationally carbamylated lysine residue and a hydroxide ion and that are bound to the protein scaffold by four histidine imidazole nitrogen atoms and one aspartate residue carboxylate oxygen atom [4–8]. The coordination geometry of the nickel ions is completed by labile water molecules, yielding one pentacoordinated Ni(II) ion with a distorted square-pyramidal geometry, and one hexacoordinated Ni(II) ion with a distorted octahedral geometry.

Urease is initially produced in the apo form, devoid of nickel ions and enzymatic activity. The apoenzyme is modified in several steps that require a dedicated set of

Author's personal copy

accessory proteins, usually comprising UreD, UreF, UreG, and UreE [2, 9]. This process leads to carbamylation of the active-site lysine and incorporation of the binuclear metallic active site, with consequent enzyme activation. The activity of urease is strictly required for the survival and growth of bacterial pathogens that colonize human and animal gastric mucosa as well as intestinal and urinary tracts, and therefore both the enzyme and the accessory proteins are targets for drug development [10, 11].

The urease activation process entails the formation of a multimeric complex between the apoenzyme and UreD, UreF, and UreG, with the latter protein likely being responsible for lysine carbamylation following GTP hydrolysis [12]. UreE appears to act as a metallochaperone by delivering Ni(II) to the UreDFG complex [13–16]. Another crucial role for UreE is the enhancement of the GTPase activity of UreG [16], which relies on the direct UreE–UreG interaction recently shown to occur in vivo and in vitro [17, 18].

Recombinant UreE proteins from different sources, including *Klebsiella aerogenes* (*Ka*UreE) [19], *Sporosarcina pasteurii* (formerly known as *Bacillus pasteurii* [20], GenBank accession code AAD55059.1, 147 residues) (*Sp*UreE) [21], and *Helicobacter pylori* (*Hp*UreE) [22, 23], have been structurally characterized and shown to be head-to-head homodimers, using the C-terminal domain for dimerization and metal binding. However, although they share common structural features, UreE proteins display different metal binding capabilities. In particular, they exhibit a variable stoichiometry for nickel binding that ranges from one metal ion bound per dimer for *Hp*UreE [17, 24] to six metal ions for *Ka*UreE [25], with two Ni(II) ions bound in the case of *Sp*UreE [26]. This different behavior can be correlated to the nature of the C-terminal regions of these different proteins: *Ka*UreE features a histidine-rich tail containing ten histidine residues among the last 15 amino acids, *Sp*UreE contains two C-terminal histidine residues at the end of its sequence in a His-Gln-His motif, and *Hp*UreE contains a single histidine residue (His^{152}) [27]. These histidine residues in the C-terminal portion suggested a role for this region in determining metal transport by UreE proteins, in terms of both the selectivity and the stoichiometry of metal binding [17, 26, 27]. Recently, the structural and functional details of these regions have been established, with the determination of the crystal structures of apo-*Hp*UreE Ni(II)-*Hp*UreE, and Zn(II)-*Hp*UreE [23]. These structures, corroborated by X-ray absorption spectroscopy data, reveal that the His^{152} residue, located in the C-terminal region of the protein, contributes to the coordination of the metal ion together with the fully conserved His^{102} residue on the protein surface (see the scheme in Fig. 1) [23]. The C-terminus in apo-*Hp*UreE in the crystalline state is generally disordered (represented by the wiggly lines in Fig. 1), but becomes

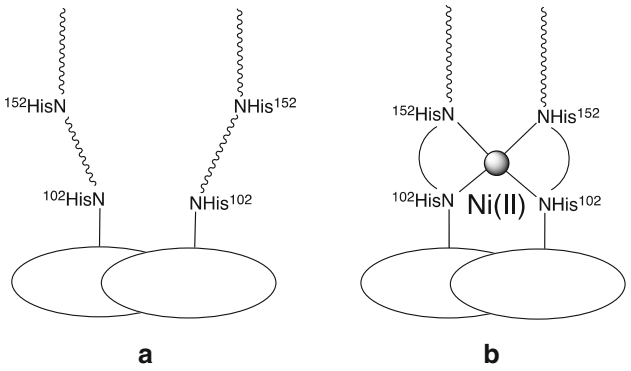

Fig. 1 Schematic representation of the crystal structure of apo-*Hp*UreE (panel **a**) and Ni-*Hp*UreE (panel **b**), showing the metal-binding role of the histidine residues in the C-terminal region of the protein

partially ordered on metal ion binding, and therefore can exist in an "open" (Fig. 1a) or a "closed" (Fig. 1b) form. It has been suggested that a conformational change between these two forms is involved in the uptake and release of metal ions from UreE proteins [21, 23].

Metal ion selectivity is a general issue concerning a large variety of processes related to metal homeostasis and cellular metal trafficking. In particular, the different affinity of UreE proteins for cognate [Ni(II)] and noncognate [e.g., Zn(II)] metal ions, together with the consequences of the different identity of the bound metal ion for the structural properties of the holoprotein, have been recently identified as key factors that modulate key cellular metabolic metal-dependent processes [28]. In this study, the affinities of *Sp*UreE for Ni(II) and Zn(II) have been determined, compared and discussed, and the structure of the protein crystallized in the presence of equimolar amounts of both metal ions has been established. Overall, the thermodynamics and structural parameters that modulate the metal ion specificity of different binding sites on the protein surface have been elucidated.

Materials and methods

Protein expression and purification

Recombinant wild-type *Sp*UreE was purified using a modification of a previously reported protocol [26]. Cells of *Escherichia coli* BL21(DE3) (Novagen) were transformed by electroporation with the pET-3d plasmid (Novagen) containing the wild type gene (pET-3d::ureE) obtained as previously described [26]. Cells were subjected to a double selection process aimed at the production of high yields of the recombinant protein [29].

The cells were grown aerobically, with vigorous stirring, at 310 K, in M9 medium [30] supplemented with

Author's personal copy

ampicillin (100 μg mL^{-1}). When the optical density at 600 nm reached 0.6–0.8, gene expression was induced by addition of 0.5 mM isopropyl thiogalactopyranoside. Cells were harvested after 16 h by centrifugation at 5,000 rpm for 30 min at 277 K, and were resuspended in 40 mL of 50 mM tris(hydroxymethyl)aminomethane (Tris)–HCl, pH 7, containing 10 mM $MgCl_2$, 2 mM dithiothreitol, and 20 μg mL^{-1} bovine pancreas DNase I. The cells were broken by two passages through a French pressure cell (SLM-Aminco) operating at 20,000 psi. Cell debris were removed by centrifugation at 15,000 rpm for 30 min at 277 K. Solid ammonium sulfate (40 % saturation) was added to the extract, and the supernatant obtained by centrifugation (15,000 rpm for 30 min at 277 K) was further treated with ammonium sulfate up to 60 % saturation. The supernatant obtained after centrifugation as described above was loaded onto a phenyl-Sepharose XK26 column (GE Healthcare) preequilibrated with 50 mM Tris–HCl buffer, pH 7, containing 2 M ammonium sulfate and 5 mM ethylenediaminetetraacetic acid (EDTA). The column was washed with the starting buffer until the baseline was straight, using a flow rate of 3 mL min^{-1}. A 300-mL linear gradient of 50 mM Tris–HCl buffer, 5 mM EDTA, pH 7, containing a decreasing concentration of ammonium sulfate (from 2 to 0 M) was applied to elute *Sp*UreE. Fractions containing *Sp*UreE (eluted at about 1.2 M ammonium sulfate) were combined and dialyzed (5-kDa molecular mass cutoff membrane) against 50 mM Tris–HCl buffer, 5 mM EDTA, pH 7. The resulting solution was applied onto a Q-Sepharose XK26 column (GE Healthcare) previously equilibrated with 50 mM Tris–HCl buffer, 5 mM EDTA, pH 7. After the column had been washed with the equilibration buffer, a 300-mL linear gradient of NaCl was applied from 0 to 1 M at 3 mL min^{-1}. Fractions containing *Sp*UreE (eluted at about 0.2 M NaCl) were combined. The fractions containing pure *Sp*UreE were tested for purity using sodium dodecyl sulfate–polyacrylamide gel electrophoresis, and using a NuPAGE Novex precast gel system (Invitrogen) and NuPAGE 4–12 % [bis(2-hydroxyethyl)amino]tris(hydroxymethyl)methane gels (Invitrogen). Staining was done using SimplyBlue SafeStain (Invitrogen). Protein quantification was performed by absorption spectroscopy, using the theoretical value of the extinction coefficient at 280 nm (21,430 M^{-1} cm^{-1}) calculated using the ProtParam tool (http://us.expasy.org/cgi-bin/protparam) and the amino acid sequence of the wild-type protein. *Sp*UreE aliquots were concentrated to approximately 17 mg mL^{-1} using Centricon ultrafiltration units (Millipore) and were stored at 193 K. The final yield of pure protein was 150–200 mg per liter of culture. The purified protein was devoid of metal ions as shown by inductively coupled plasma optical emission spectroscopy as previously described [26]. Throughout this article, the protein concentration provided is referred to the homodimer.

Isothermal titration calorimetry experiments

Direct and reverse titration experiments were performed at 298 K using a high-sensitivity VP-ITC microcalorimeter (MicroCal, Northampton, MA, USA). *Sp*UreE, purified as described in the previous section, was eluted from a Superdex-75 size-exclusion column, using 20 mM Tris–HCl buffer, 150 mM NaCl, pH 7, immediately before the isothermal titration calorimetry (ITC) measurement to exchange the buffer and to freshly purify the protein. *Sp*UreE and the metal ions (from 100 mM stock solutions) were diluted using the same buffer. The measuring cell contained 1.4093 mL of either *Sp*UreE or metal ion solution for direct or reverse titrations, respectively, and the reference cell was filled with deionized water. Before starting the experiments, we verified the baseline stability. A time of 300–360 s between injections was applied in order to allow the system to reach thermal equilibrium after each addition. For each titration, a control experiment was performed by adding the titrating protein or metal ion solution to the buffer alone, under identical conditions. The heats of dilution were negligible. In the case of direct titrations, an *Sp*UreE solution (15 μM dimer) in the cell was titrated with 55 injections (5 μL each) of $NiSO_4$ or $ZnSO_4$ solutions (0.5 mM). In the case of reverse titrations, the $NiSO_4$ or $ZnSO_4$ solutions (20 μM) were titrated with 25 [for Ni(II)] or 40 [for Zn(II)] injections (10 μL each) of a solution containing 70–80 μM *Sp*UreE dimer. In the case of Zn(II) titration, three subsequent experiments were performed to reach binding saturation, with the syringe being refilled with the protein solution and the titration being continued. The three binding curves were then concatenated into a single curve using the program ConCat32 (MicroCal). For competition experiments, *Sp*UreE (19 μM) was incubated in the cell with an equimolar concentration of Ni(II) [or Zn(II)] and was titrated with 55 injections (5 μL each) of 0.5 mM Zn(II) [or Ni(II)] solution in the syringe. The integrated heat data were analyzed using the Origin software package (MicroCal), and were fitted using a non-linear least-squares minimization algorithm to theoretical titration curves that involved different binding models. The reduced parameter χ^2_v ($\chi^2_v = \chi^2/N$, where N is the number of degrees of freedom, $N = N_{idp} - N_{par}$, where N_{idp} is the number of points and N_{par} is number of parameters floating in the fit) was used to establish the best fit among the models tested. The values for the enthalpy change of the reaction (ΔH), the binding affinity constant (K_b), and the number of sites (n) were the parameters of the fit. The reaction entropy was calculated using the equations $\Delta G = -RT\ln K_b$ ($R = 1.9872$ cal · mol^{-1} K^{-1}, $T = 298$ K) and $\Delta G = \Delta H - T\Delta S$. The

Author's personal copy

dissociation constants and thermodynamic parameters provided in this study do not take into account possible proton transfer events linked to metal binding, as such a treatment is beyond the scope of this study. However, the values of the measured equilibrium constants compare well with those reported in the literature and determined using equilibrium dialysis coupled with metal analysis, which, in principle, should also take into account similar effects [26]. The statistics of the fitting analysis of the ITC experiments on Ni(II) and Zn(II) binding are summarized in Table 1.

Crystallization, X-ray data collection, structure determination, and refinement

*Sp*UreE, purified as described earlier, was eluted from a Superdex-75 size-exclusion column using 20 mM Tris–HCl buffer, 150 mM NaCl, at pH 8, and concentrated to 5.3 mg mL^{-1}. This protein solution was incubated with 2.5 molar equivalents of Ni(II) ($NiSO_4$) and Zn(II) ($ZnSO_4$). Crystals of *Sp*UreE were obtained from this solution using the sitting drop vapor diffusion method in the presence of reservoir precipitant solution containing 0.06 M $MgCl_2/CaCl_2$, 0.1 M sodium *N*-(2-hydroxyethyl)piperazine-*N*′-ethanesulfonic acid/3-(*N*-morpholino)propanesulfonic acid pH 7.5, 20 % ethylene glycol, and 10 % PEG 8,000. A single crystal was selected and used to collect X-ray diffraction data on beamline 14.1 at the Berliner Elektronenspeicherring-Gesellschaft für Synchrotronstrahlung (BESSY). Three data sets were collected at 0.918 Å (native data), 1.282 Å (near the peak absorption at the Zn K edge), and 1.485 Å (near the peak absorption at the Ni K edge). The absorption peaks were determined directly from the crystal by scanning the X-ray energy and observing the fluorescence with a Roentec X-Flash detector. Each diffraction image was obtained by irradiating the crystal for 10 s while rotating it by 0.5°. Data covering 130° were collected for the native data set, 100° at the zinc anomalous edge, and 180° at the nickel edge. The diffraction data were processed with XDS [31]. The native data obtained at 1.88-Å resolution were used to solve the crystal structure by molecular replacement, using Phaser [32] and the coordinates of *Sp*UreE (Protein Data Bank code 1EB0) [21] as the starting model. The model was refined using Refmac [33] with separation of two twin domains (twin fractions 0.741 and 0.259, twin operators H, K, and L and K, H, and −L, respectively). The same procedure of molecular replacement and refinement was applied independently also to the other two data sets, collected at wavelengths near the peak absorption of the nickel K edge and the zinc K edge in order to remove any systematic phase bias in comparing the X-ray anomalous difference electron density maps. The program COOT was used for structure building [34]. The statistics of the X-ray data collection and refinement are summarized in Table 2. The structure has been deposited in the Protein Data Bank with accession code 4L3K. Figures representing protein structures were constructed using PyMOL (http://www.pymol.org/).

Results and discussion

The nickel binding properties of *Sp*UreE, previously determined by us through the direct measurement of free and bound metal ion concentrations at dialysis equilibrium using inductively coupled plasma optical emission spectroscopy, and supported by X-ray absorption spectroscopy, involve the presence of two sites per protein dimer, with the Ni(II) ions in octahedral coordination geometry and an average of two histidine residues and four O/N ligands bound to each metal ion [26]. Previous nickel binding data for *Sp*UreE obtained using equilibrium dialysis, and measuring the radioactivity of ^{63}Ni, were interpreted as indicating the binding of three Ni(II) ions per dimer [35], but this analysis was later shown to be flawed [26], and inconsistent with subsequently reported observations [36]. The involvement of the C-terminal portion of *Sp*UreE in the binding of Ni(II), and in particular the role of His^{145} and His^{147}, was indicated [35] by the disappearance of their NMR signals caused by binding of the Ni(II) ions established to be paramagnetic high spin ($S = 1$) in octahedrally coordinated sites [37].

Two possible models were then used to fit the binding data (see Fig. 2).

One model (Fig. 2a) involved the presence of two identical metal sites with negative cooperativity ($K_{d1} = 1.4$ μM and $K_{d2} = 25$ μM), whereas the alternative model (Fig. 2b) assumed the presence of two different binding sites featuring different affinity for Ni(II) ($K_{d1} = 0.7$ μM and $K_{d2} = 50$ μM) and unresolved cooperativity [26]. In the first model, each metal ion is bound to the conserved His^{100} and to either of the two histidine residues found at the C-terminal portion of each monomer, His^{145} or His^{147}. In the second model, one Ni(II) ion is bound to one His^{100} from each monomer, and the second Ni(II) ion is bound to a pair of His^{145} residues or a pair of His^{147} [26] residues. In the absence of additional structural information, no conclusion as to which of the two models is correct could be reached. Here, we used ITC and X-ray crystallographic data to reevaluate the thermodynamics parameters and the molecular details of Ni(II) binding to *Sp*UreE. Concomitantly, a comparison with Zn(II) binding was carried out to sort out the possible determinants of metal ion specificity featured by this metallochaperone.

Author's personal copy

Table 1 Results of the fitting analysis of isothermal titration calorimetry experiments on Ni(II) and Zn(II) binding to *Sp*UreE

Binding scheme	χ^2_v	n	K_b (M^{-1})	ΔH (kcal mol^{-1})	ΔS (cal mol^{-1} K^{-1})
Ni(II) binding to homodimeric apo-*Sp*UreE					
One set of sites	6.9×10^4	2.1 ± 0.1	$(1.8 \pm 0.2) \times 10^7$	-6.0 ± 0.1	13
Two sets of Ni(II) sites	7.8×10^4	$n_1 = 1.1 \pm 1.2$	$(1.4 \pm 15) \times 10^7$	$-23 \pm 8{,}400$	-45.1
		$n_2 = 1.0 \pm 1.2$	$(2.6 \pm 60) \times 10^7$	$15 \pm 9{,}800$	82.4
Sequential binding of two Ni(II) ions	6.4×10^4	$n_1 = 1.0$	$(6.0 \pm 2.6) \times 10^5$	3.2 ± 3.1	37.3
		$n_2 = 1.0$	$(2.3 \pm 0.9) \times 10^7$	-15.0 ± 0.3	-16.7
Zn(II) binding to homodimeric apo-*Sp*UreE					
One set of sites	NA	NA	NA	NA	NA
Two sets of Zn(II) sites	7.9×10^4	$n_1 = 0.6 \pm 0.3$	$(5.8 \pm 6.2) \times 10^4$	10.2 ± 10.1	55.9
		$n_2 = 0.54 \pm 0.01$	$(3.9 \pm 2.9) \times 10^7$	-17.3 ± 0.1	-23.4
Sequential binding of two Zn(II) ions	NA	NA	NA	NA	NA
Sequential binding of two *Sp*UreE dimers to one Zn(II) ion	4.5×10^4	$n_1 = 1.0$	$(1.1 \pm 0.2) \times 10^7$	-5.4 ± 0.2	14.3
		$n_2 = 1.0$	$(4.6 \pm 0.4) \times 10^6$	-12.4 ± 0.2	-11.0
Ni(II) binding to Zn(II)-bound *Sp*UreE					
Sequential binding of two Ni(II) ions to one Zn(II)-bound *Sp*UreE dimer	3.4×10^3	$n_1 = 1.0$	$(2.4 \pm 0.3) \times 10^5$	-2.9 ± 0.1	15.0
		$n_2 = 1.0$	$(1.1 \pm 0.3) \times 10^3$	-15.8 ± 0.4	-39.3

NA not acceptable statistics

Nickel binding investigated by ITC

The ITC measurements were initially conducted by performing a direct titration, namely, by adding Ni(II) to the apoprotein, and the occurrence of a binding event was revealed by the presence of exothermic peaks that followed each addition (see Fig. S1a). At the protein concentrations used for this type of experiment, *Sp*UreE is reported to be a dimer in the presence of Ni(II) [35, 37]. Fits of the integrated heat data (Fig. S1b), attempted assuming a single set of identical sites, multiple sets of noninteracting sites, or a stepwise binding model, consistently yielded poor results characterized by an unrealistically low stoichiometry or negative binding constants (see Table 1). Considering the previously determined Ni(II)–dimer 2:1 stoichiometry for *Sp*UreE, together with the observation of a rather featureless binding curve, as well as saturation of binding that occurs at very low metal binding stoichiometry, we suspected the presence of positive cooperativity. Positive cooperativity can generally be resolved using a reverse titration method [38, 39]. Figure 3a shows a representative plot of raw titration data reporting the thermal effect of injecting *Sp*UreE into a solution of $NiSO_4$, and Table 1 summarizes the results of the analysis. The integrated heat data, shown in Fig. 3b, were initially fitted using a model involving a single set of identical and independent Ni(II) binding sites. This fit yielded $\chi^2_v = 6.9 \times 10^4$, stoichiometry $n = 2.1 \pm 0.1$ Ni(II) ions per dimer, $K_b = 1.8 \pm 0.2 \times 10^7$ M^{-1} ($K_d = 56 \pm 6$ nM), $\Delta H = -6.0 \pm 0.1$ kcal mol^{-1}, and $\Delta S = 13.0$ cal mol^{-1} K^{-1}. The fit using an alternative model involving two independent and different binding sites produced a similar value for χ^2_v (7.8×10^4), but yielded two very similar binding constants ($1.4 \pm 15 \times 10^7$ M^{-1} and $2.6 \pm 60 \times 10^7$ M^{-1}) with unacceptably large errors in the stoichiometry (1.1 ± 1.2 and 1.0 ± 1.2) and thermodynamic parameters, indicating an overparameterization of the model, and was thus discarded. A third model, involving two sequential steps of single ion binding ($n = 1$) was also considered, and resulted in $\chi^2_v = 6.4 \times 10^4$, $K_{b1} = 6.0 \pm 2.6 \times 10^5$ M^{-1} ($K_d = 1.7 \pm 0.7$ μM), $\Delta H_1 = 3.2 \pm 3.1$ kcal mol^{-1}, $\Delta S_1 = 37.3$ cal mol^{-1} K^{-1}, $K_{b2} = 2.3 \pm 0.9 \times 10^7$ M^{-1} ($K_d = 43 \pm 17$ nM), $\Delta H_2 = -15.0 \pm 0.3$ kcal mol^{-1}, and $\Delta S_2 = -16.7$ cal mol^{-1} K^{-1}. This model implies large positive cooperativity, with the second binding constant increasing approximately 40-fold as compared with the first binding constant. These parameters are characterized by relatively larger errors in the thermodynamics of the first binding site, but feature similar statistics as compared with the first model. In addition, the presence of such a large positive cooperativity would explain the peculiar shape of the curve and the difficult interpretation of the direct titration experiment, making this latter fitting model more consistent, overall, with the data obtained. The difficulty in analyzing the data using direct calorimetric titrations can explain the different conclusions

Author's personal copy

Table 2 X-ray diffraction data collection and refinement statistics

	*Sp*UreE native data	Zn K edge data	Ni K edge data
BESSY beamline	14.1	14.1	14.1
Temperature (K)	100	100	100
Wavelength (Å)	0.91841	1.28248	1.48503
Space group	$P6_3$		
Cell constants (Å)	$a = b = 91.329$, $c = 82.792$		
Resolution (Å)	1.88–45.66 (1.88–1.98)	2.10–45.77 (2.10–2.21)	2.49–45.80 (2.49–2.63)
R_{sym}[a] (%)	6.9 (91.5)	4.8 (59.0)	7.0 (91.7)
$I/\sigma(I)$	18.20 (2.21)	16.76 (2.05)	18.50 (2.03)
Completeness (%)	99.7 (98.5)	98.7 (96.5)	99.7 (98.6)
Redundancy	6.6 (6.5)	3.2 (3.1)	5.7 (5.6)
Matthew coefficient (Å^3 Da^{-1})	2.95		
Solvent content (%)	58		
Refinement			
Number of reflections in working set	30,497		
Number of reflections in test set	1,544		
R_{work}/R_{free} (%)	17.07/20.73		
Number of protein atoms	2,292		
Number of metal ions	2		
Number of water molecules	161		
Average *B* factor for protein atoms (Å^2)	34.18		
Average *B* factor for metal ions (Å^2)	38.59		
RMSD of bond length (Å)	0.019		
RMSD of bond angles (°)	2.157		
Residues in most favorable regions (%)	90.4		
Residues in additionally allowed regions (%)	8.8		
Residues in generously allowed regions (%)	0.4		
Residues in disallowed regions (%)	0.4		

Values in *parentheses* are for the highest-resolution shell

BESSY Berliner Elektronenspeicherring-Gesellschaft für Synchrotronstrahlung, *RMSD* root mean square deviation

[a] $R_{sym} = \Sigma_{hkl}\Sigma_i|I_i(hkl) - \langle I(hkl)\rangle|\Sigma_{hkl}\Sigma_i I_i(hkl)$, where $I_i(hkl)$ is the integrated intensity of a given reflection and $\langle I(hkl)\rangle$ is the mean intensity of multiple corresponding symmetry-related reflections

that can be drawn here as compared with those obtained using the same direct titrations with dialysis and metal analysis, which were interpreted using negative cooperativity [26]. Moreover, previous data obtained using ITC on the same protein, interpreted with two sequential binding events, each with $n = 1$, and yielding dissociation constants of $K_{d1} = 0.8$ μM and $K_{d2} = 50$ μM, were affected by much lower overall quality [36]. In the case of similar calorimetric titrations performed with *Hp*UreE, a single binding site for Ni(II) was observed, with K_d in the micromolar range [17]. A notable difference between *Hp*UreE and *Sp*UreE, which could explain the different stoichiometry and thermodynamics of Ni(II) binding, is the presence of a single histidine residue in the C-terminal arm of *Hp*UreE (His^{152}), whereas two histidines are found in *Sp*UreE (His^{145} and His^{147}) in addition to the conserved His^{102} (for *Hp*UreE) and His^{100} (in *Sp*UreE) [27]: in the case of *Hp*UreE, Ni(II) binds to a pair of His^{102} residues and a pair of His^{152} residues, as observed by crystallography and X-ray absorption spectroscopy (see Fig. 1b) [23]. In the case of *Sp*UreE, the first micromolar binding event could involve His^{145} and His^{147} (low-affinity site), causing a reorganization of the disordered C-terminal arms of the protein, moving the two His^{145} residues on the two arms closer to each other and to the two His^{100} residues, bringing about a nanomolar binding event involving His^{100} and His^{145} (high-affinity site). In this way, the two distal histidine residues would act as a molecular funnel to collect and direct Ni(II) ions onto the putatively functional binding high-affinity site involving the pair of His^{100} residues. Alternatively, the low-affinity event could involve His^{100} and His^{145}, bringing the two His^{147} residues closer to each other and causing the formation of the second, high-affinity binding site. Titrations of apo-*Sp*UreE and nickel-loaded

Author's personal copy

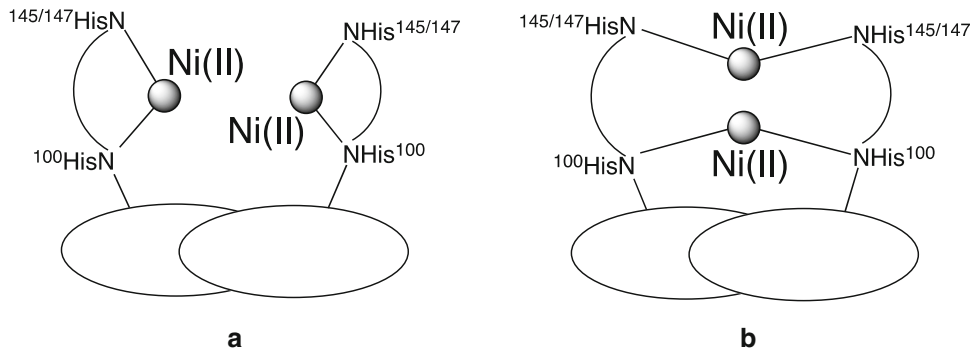

Fig. 2 Schematic representation of the Ni(II) binding modes by *Sp*UreE used to fit the data obtained by equilibrium dialysis experiments in Ref. 26

*Sp*UreE with Zn(II), as well as X-ray crystallography, helped us to resolve this issue, as detailed below.

Zinc binding investigated by ITC

To compare the different affinity of *Sp*UreE for Ni(II) and Zn(II), the thermodynamics of zinc binding were also investigated using the same method. Similarly to what observed in the case of the titration with Ni(II), the direct titration of Zn(II) into the apoprotein solution showed the occurrence of a binding event, revealed by exothermic peaks that followed each injection (Fig. S2a), but the integrated heat data (Fig. S2b) could not be reliably fit using any of the binding models, consistently yielding poor results characterized by an unrealistically low stoichiometry. Previous zinc binding data collected on *Sp*UreE using the same calorimetric technique in a direct titration were interpreted using a single type of binding site with unresolved stoichiometry ($n = 1$ or 2) and an average $K_b = 9.8 \pm 0.7 \times 10^3\ M^{-1}$ binding constant [36]. We could not reproduce the same data, which were, again, of poor quality. Therefore, as in the case of nickel binding, we performed the reverse titration, with the data shown in Fig. 4a. The occurrence of an exothermic effect following each addition of *Sp*UreE to the metal solution was observed, with the resulting integrated heat data (Fig. 4b) indicating the presence of at least two different binding events and thus ruling out the single set of sites model. Modeling the curve using a sequential set of two binding events with a single Zn(II) ion bound to the *Sp*UreE dimer in each event did not lead to an acceptable fit. Attempts to fit the data using two sets of sites with different stoichiometry of Zn(II) binding to *Sp*UreE yielded the following results, characterized by large uncertainties in the fitted parameters: $\chi^2_v = 7.9 \times 10^4$, $n_1 = 0.6 \pm 0.3$, $K_{b1} = 5.8 \pm 6.2 \times 10^4\ M^{-1}$ ($K_d = 17 \pm 18\ \mu M$), $\Delta H_1 = 10.2 \pm 10.1$ kcal mol^{-1}, $\Delta S_1 = 55.9$ cal mol^{-1} K^{-1}, $n_2 = 0.54 \pm 0.01$, $K_{b2} = 3.9 \pm 2.9 \times 10^7\ M^{-1}$ ($K_d = 26 \pm 19$ nM), $\Delta H_2 = -17.3 \pm 0.1$ kcal mol^{-1}, and $\Delta S_2 = -23.4$ cal mol^{-1} K^{-1}. Regardless of the precision of the fit, the two binding events observed for Zn(II) show a half-integer stoichiometry, suggesting that, in the experimental conditions used, the dimeric *Sp*UreE forms a dimer of dimers in the presence of Zn(II). Therefore, we fitted the data using a model that considered the sequential binding of two *Sp*UreE dimers to a single Zn(II) ion. The fit obtained

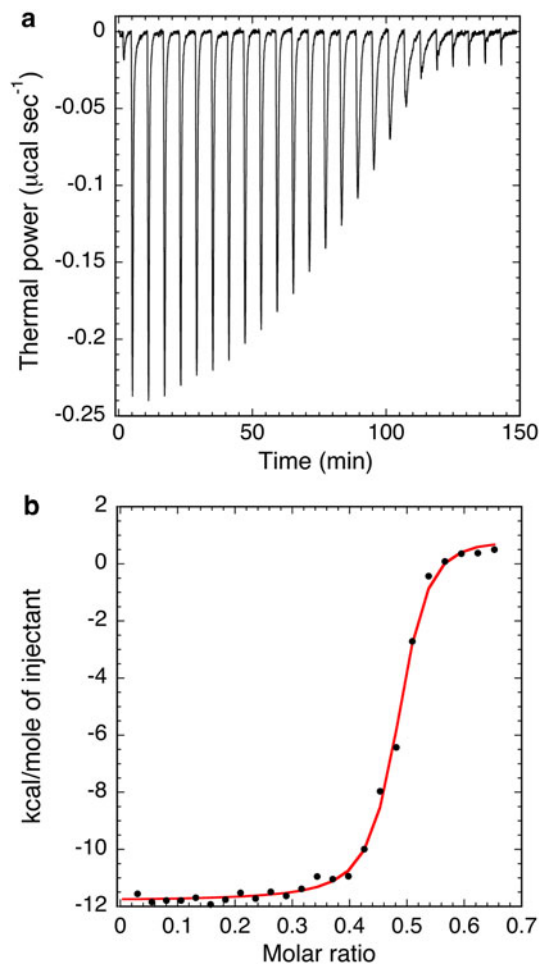

Fig. 3 Nickel binding properties of *Sp*UreE determined using isothermal titration calorimetry. **a** Representative plot of raw inverse titration data of Ni(II) (20 μM) with *Sp*UreE (70 μM). **b** Integrated heat data as a function of metal/protein molar ratio. The *continuous line* represents the best fit obtained using a model involving sequential binding of two Ni(II) ions

Author's personal copy

(Fig. 4b) resulted in improved statistics and smaller errors on the thermodynamics parameters: $\chi^2_v = 4.5 \times 10^4$, $K_{b1} = 1.1 \pm 0.2 \times 10^7\ M^{-1}$ ($K_{d1} = 91 \pm 16$ nM), $\Delta H_1 = -5.4 \pm 0.2$ kcal mol^{-1}, $\Delta S_1 = 14.3$ cal mol^{-1} K^{-1}, $K_{b2} = 4.6 \pm 0.4 \times 10^6\ M^{-1}$ ($K_{d2} = 217 \pm 19$ nM), $\Delta H_2 = -12.4 \pm 0.2$ kcal mol^{-1}, and $\Delta S_2 = -11.0$ cal mol^{-1} K^{-1}). This model (Fig. 5) is consistent with the crystallographic observation of a dimer of dimers of *Sp*UreE bridged by a single Zn(II) ion bound to four His^{100} residues and two water molecules [21], further supporting its reliability.

The slightly negative cooperativity deduced from the fit could be explained by steric hindrance between the two protein dimers bound to the same Zn(II) ion, as also revealed by the crystal structure [21]. This observation marks a distinctly different behavior of *Sp*UreE in the presence of Ni(II) and Zn(II), with the two metal ions possibly modulating in different ways the chaperone function of the protein.

Metal binding investigated by X-ray crystallography

So far, all attempts to obtain a crystal of Ni(II)-bound *Sp*UreE suitable for crystallography, using different metal-to-protein ratios, have failed. Soaking of the Zn(II)-bound *Sp*UreE crystals, containing a dimer of dimers bridged by Zn(II) itself, led to the observation of either substitution of Zn(II) by Ni(II) in this oligomeric form (detected by anomalous scattering) or the dissolution of the crystal, probably due to the rupture of the dimer of dimers and subsequent increase of the solubility of the Ni(II)-bound protein [21], or protein precipitation in the presence of large excess of Ni(II). In this study, to provide structural support for the calorimetric metal binding data, we attempted the co-crystallization of *Sp*UreE in the presence of both Ni(II) and Zn(II) added in equimolar amounts. This experiment allowed us to obtain diffracting crystals, which were used to provide structural support for the aforementioned models drawn on the basis of the calorimetric metal competition data. Crystallographic data analysis (see Table 2) resulted in the modeling of two protein chains in the asymmetric unit. The overall polypeptide fold is similar to that previously reported [21]: each monomer is made of two domains, N- and C-terminal, connected by a flexible linker (Lys^{74}–Lys^{77}), with the N-terminal domain constituted by two three-stranded mixed β-sheets that stack upon each other in a nearly perpendicular orientation, and the C-terminal domain made of a four-stranded antiparallel β-sheet and two α-helices organized in a ferredoxin-like βαββαβ fold (Fig. 6a). The C-terminal domains are responsible for head-to-head dimerization contacts stabilized by hydrophobic interactions formed between α-helices. However, in contrast to the previously observed dimer-of-dimers arrangement in the crystal [21], the protein chains do not form a dimer of dimers in the crystal lattice, but simply dimers arranged around the 6_3 axis, forming a large solvent channel (Fig. 6b).

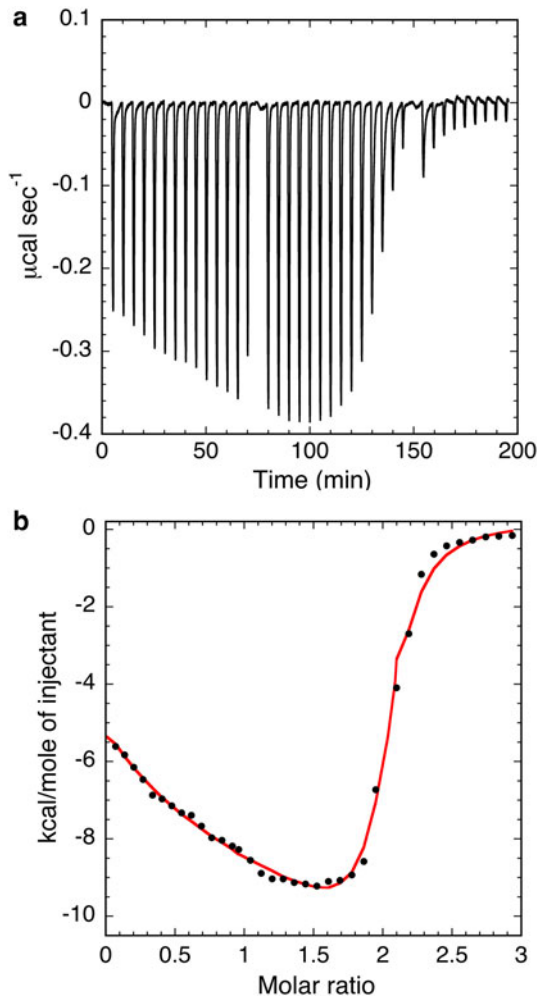

Fig. 4 Zinc binding properties of *Sp*UreE determined using isothermal titration calorimetry. **a** Representative plot of raw inverse titration data of Zn(II) (20 µM) with *Sp*UreE (80 µM). **b** Integrated heat data as a function of the metal-to-protein molar ratio. The *continuous line* represents the best fit obtained using a model involving two independent sets of binding sites for Zn(II)

Two metal binding sites were detected in the structure (Fig. 6a). One is located on the surface of the protein, in a central position between the two protomers of the dimer (site 1), on the peripheral surface of the *Sp*UreE dimer. The coordination environment of the bound metal ion is consistent with octahedral geometry, but only two of its ligands can be identified unambiguously. These are the two conserved and adjacent His^{100} Nε, one from each chain, which form an angle of approximately 90° with the metal ion. Each His^{100} is stabilized by a hydrogen bond formed between His^{100} Nδ and Asn^{98} Oδ from the neighboring

Author's personal copy

chain, stabilizing the homodimer (Fig. 7). The electron density for the Tyr[142], Arg[143], and Gly[144] residues is weak, because of disorder, in both chains A and B, and only the main chain can be tentatively traced. Residual electron density is most likely to correspond to the two His[145] residues, one from each chain of the monomer, bound to the metal ion (Fig. 7). This is consistent with what was observed in the case of *Hp*UreE, in which a pair of histidine residues (His[152]) from the two C-terminal portions of the protein were found coordinated to Ni(II) in addition to His[102], corresponding to His[100] in *Sp*UreE [23]. The two remaining ligands required to complete the octahedral geometry, on the side exposed to the wide solvent channel in the crystal lattice, are not visible in the electron density map. These ligands were suggested to be water molecules in the case of *Hp*UreE on the basis of X-ray absorption spectroscopic data [23]. The last two residues of the polypeptide chain, Gln[146] and His[147], were not observed, owing to disorder. This is consistent with the observation that, also in *Hp*UreE, the last 18 residues that follow the Ni(II)-bound His[152] are disordered [23]. The results obtained using ITC in solution indicate that His[147] could be involved in binding of a second Ni(II) ion, which, however, is not visible in the crystal structure. The explanation for this could be related to the lower affinity of this distal site for Ni(II). Alternatively, the protein disorder involving the protein C-terminal arm observed in the crystalline state could prevent the observation of the His[147] electron density, thus precluding a metal ion bound to this residue from being visible in the diffraction map.

The second metal ion (site 2) was found in the N-terminal domain, linking symmetry-related dimers, and coordinated with a pseudo-tetrahedral geometry, interacting with His[9] and Asp[12] as well as with the corresponding His[9*] and Asp[12*] residues from a symmetry-related dimer (Fig. 8).

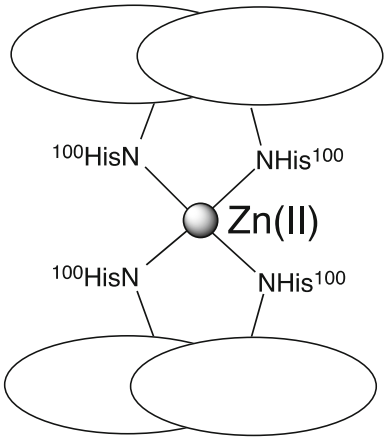

Fig. 5 Schematic representation of the dimer of dimers of *Sp*UreE binding one Zn(II) ion, as derived from ITC (this work) and crystallographic studies (Ref. 21)

Site 1 has been always assumed to be the location of physiological Ni(II) binding and release implied in the metallochaperone role of UreE. This site has also been observed to bind Zn(II) in *Sp*UreE [21] as well as Cu(II) in *Ka*UreE*, a C-terminal truncated form of the native *Ka*UreE [19]. On the other hand, site 2 has never been described previously, and it is formed by two neighboring *Sp*UreE dimers in the crystal lattice (Fig. 8a). It is unlikely that the *Sp*UreE molecules in dilute solution form such stable contacts between two dimers, and therefore this interaction is likely to be an artifact of crystallization. Moreover, calorimetric measurements indicate that, in the case of Ni(II), a 1 + 1 stoichiometry per protein dimer is observed, whereas Ni(II) binding to sites 2 in the dimeric protein, in addition to site 1, would create a 1 + 2 stoichiometry. In the case of Zn(II), the 2:1 stoichiometry between the *Sp*UreE dimer and the metal ion determined by calorimetry is not compatible with Zn(II) binding to site 2 in the tetrameric quaternary structure observed in the crystallization experiments.

Ni(II) and Zn(II) competition for *Sp*UreE

A comparison of the occupancy of the two sites in the presence of an equimolar Ni(II) and Zn(II) mixture offers an interesting opportunity to assess their relative affinities for the two metal ions. For this purpose, anomalous difference maps were calculated from diffraction data obtained using wavelengths at the zinc and nickel absorption K edges using the anomalous amplitudes, $|F_+ - F_-|$, and phases calculated from the refined atomic models and retarded by 90°. The maps showed outstanding peaks in both site 1 and site 2 and no significant peaks elsewhere (Fig. 9). In the nickel K edge data, the peak in site 1 had a height of 12.9 root mean square deviation (RMSD) and the peak at site 2 was at 9.2 RMSD. On the other hand, in the zinc K edge data, the peak in site 1 was at 8.1 RMSD, and the peak at site 2 was at 29.6 RMSD. These anomalous X-ray data indicated that the Ni(II) and Zn(II) ions are bound differently in two distinct metal binding sites of *Sp*UreE, and the following analysis could help to quantify the relative occupancies. First, the measurement at the nickel absorption edge should be sensitive to nickel but not to zinc, because the X-ray energy at the nickel absorption edge is too low to excite zinc. Next, the X-ray energy at the zinc K edge should excite primarily the Zn(II) ions, but it will also excite nickel to some extent. The relative strength of the nickel and zinc signals cannot be quantified easily, mainly because of prominent white lines observed in the experimental spectrum at the absorption peaks of both of these elements. This departure from the theoretical spectrum, due to interactions of the anomalous scatterer with neighboring atoms, is prominent but difficult to measure in

Author's personal copy

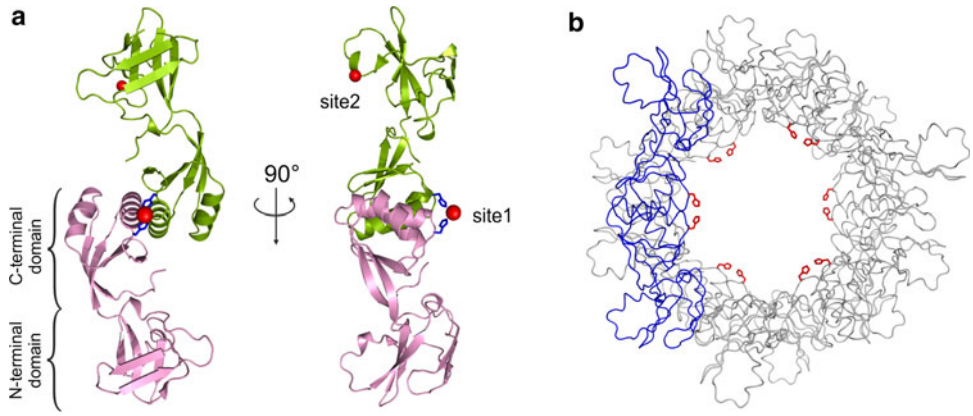

Fig. 6 **a** Ribbon diagram of the crystallographic structural model of the *Sp*UreE dimer shown in two perspectives. Polypeptide chains A and B are shown in *green* and *pink*, respectively, metal ions are shown as a *red ball*, and the two His[100] residues are shown as *blue sticks*. **b** Packing of *Sp*UreE dimers in the crystal lattice. Pairs of His[100] residues are shown in *red*

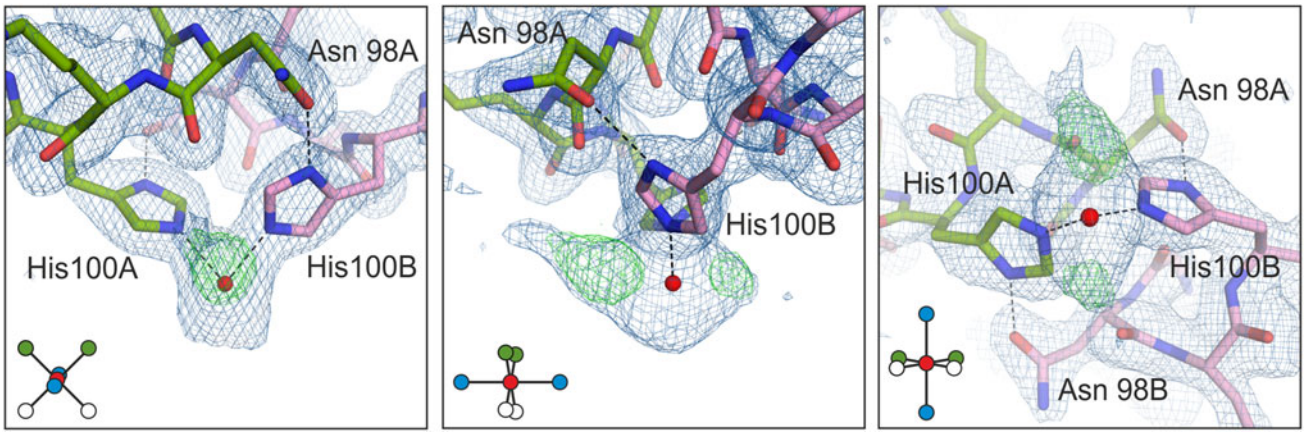

Fig. 7 Details of the nickel binding site in the center of the *Sp*UreE dimer. Three views are presented, with *insets* illustrating the octahedral geometry around the metal ion: the latter is represented by a *red sphere*, the two His[100] residues are represented by *green spheres*, and the presumed positions of the two His[145] residues are represented as *blue spheres*; *white spheres* illustrate missing interactions in the octahedral geometry. The $2F_o - F_c$ electron density map is contoured at the 1σ level (*blue*), and the $F_o - F_c$ electron density map is contoured at the 3σ level (*green*)

a normal X-ray diffraction experiment. However, some conclusions can be drawn from the observed X-ray fluorescence at the two absorption edges and the two well-defined peaks in the corresponding electron density maps. In the hypothetical case that only Zn(II) was bound in the two sites, peaks should be observed in the zinc anomalous map and no peaks should be observed in the nickel anomalous map. If only Ni(II) was bound in the two sites, peaks should be observed in both maps and the peak heights should be proportional between the two maps. This is clearly not the case, and in the presence of both Zn(II) and Ni(II) in the two sites, one can expect different proportions of peak sizes in the two maps, which is indeed the case. Going further, the occupancies of Ni(II) and Zn(II) in sites 1 and 2 can be estimated considering that (1) in the nickel anomalous map, the relative strength of the nickel signals for sites 1 and 2 is 12.9:9.2, (2) in the zinc anomalous map the combined zinc and nickel signals in sites 1 and 2 have a relative strength of 8.1:29.6. If one assumes that the combined occupancy of each site is 1, it can be calculated that the occupancy of Ni(II) in site 1 lies in the range 0.90–1.0, whereas in site 2 it is in the 0.63–0.71 range. Consequently, the occupancy of Zn(II) for site 1 is in the 0.0–0.10 range, and for site 2 is in the 0.29–0.37 range. One can thus conclude that the conserved binding site in *Sp*UreE is highly selective for Ni(II) and the other site is not selective, with Ni(II) and Zn(II) binding with similar affinity. The coordination spheres around the two sites also provide some evidence as to the identity of the bound metal ion. Site 2 is clearly tetrahedral, which is the preferred coordination of Zn(II), whereas the coordination sphere around site 1, although partly disordered, is indicative of an octahedral coordination, preferred by Ni(II). The observed overlap in the nickel and zinc binding in site 1 and site 2 suggested the implementation of competition experiments monitored by calorimetry.

As described above, calorimetric experiments show that a dimer of *Sp*UreE binds Ni(II) with 1 + 1 stoichiometry

Author's personal copy

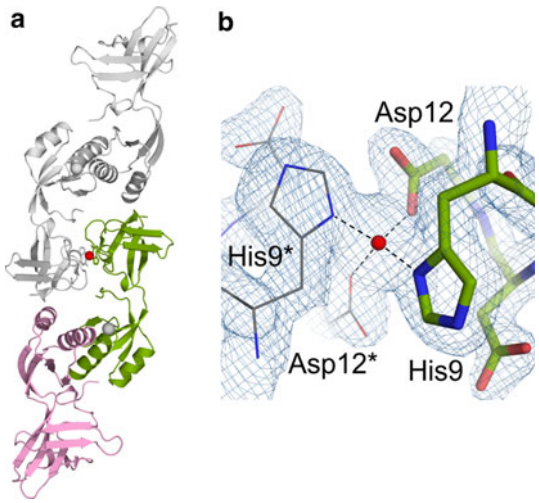

Fig. 8 The metal binding site in the N-terminal domain. **a** Two symmetry-related *Sp*UreE dimers interact with the metal ion, shown as a *red ball*. **b** Details of metal binding. The $2F_o - F_c$ electron density map is contoured at the 1.5σ level

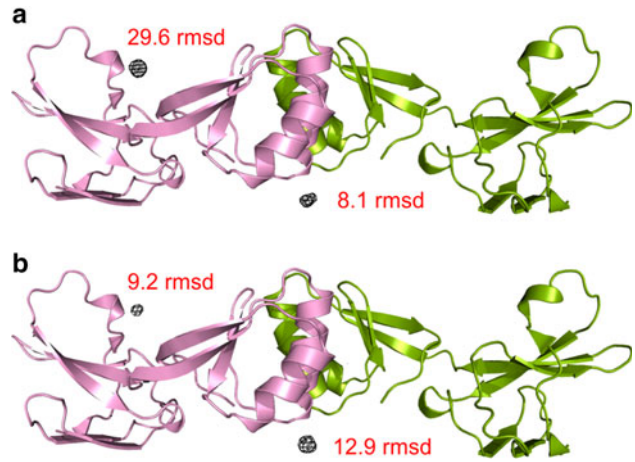

Fig. 9 Anomalous electron density maps contoured at the 4σ level for **a** zinc K edge data and **b** nickel K edge data. Heights of the peaks at the two metal ion binding sites are indicated in root mean square deviation (*rmsd*) units

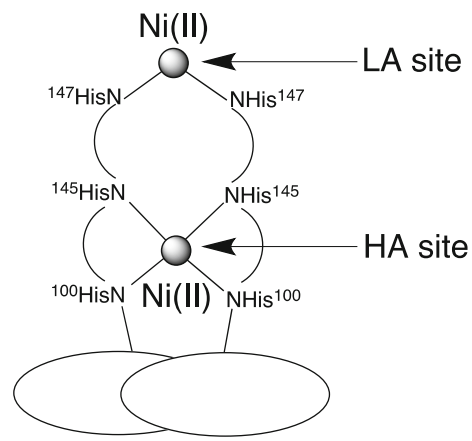

Fig. 10 Schematic representation of Ni(II) binding to the high affinity (*HA*) and low affinity (*LA*) sites of the *Sp*UreE dimer, as derived from ITC and crystallographic studies

and positive cooperativity, in a low-affinity site and a high-affinity site that involve either the His^{100}–His^{145} pair or the His^{145}–His^{147} pair. In particular, the first binding event has $K_{d1} = 1.7$ μM (low-affinity site) and the second event has $K_{d2} = 43$ nM (high-affinity site). The same approach was used to establish that two dimers of *Sp*UreE bind Zn(II) with $K_d = 91$ nM, most likely in the crystallographically established site that comprises His^{100} [21]. These values suggest that the high-affinity site for Ni(II) is the crystallographically observed site 1, involving His^{100} and His^{145}, consistent with the anomalous scattering analysis that indicates that Ni(II) binds to site 1 better than Zn(II). Consequently, the Ni(II) binding event at the low-affinity site involves His^{145} and His^{147}, confirming a storage and molecular funnel role for the C-terminal portions of UreE proteins [27] (Fig. 10).

To confirm the metal selectivity of the high-affinity site in solution, we titrated Ni(II) into a solution containing *Sp*UreE preincubated with 1 equiv of Zn(II) per protein dimer and vice versa, and monitored the reaction using ITC. The absence of significant heat of reaction in the experiment involving titration of Zn(II) into Ni(II)-bound *Sp*UreE (Fig. S3) confirmed that the Ni(II) bound to the high-affinity site of *Sp*UreE prevents Zn(II) from binding to the protein in the same site, highlighting the metal ion specificity of the high-affinity metal site for Ni(II) as compared with Zn(II). Moreover, this observation demonstrates that, in the absence of Ni(II), Zn(II) binding occurs at the high-affinity site. On the other hand, when Ni(II) is added to *Sp*UreE containing Zn(II) in the high-affinity site, exothermic peaks are observed following each injection (Fig. 11a), indicating that Ni(II) can outcompete Zn(II) for binding to the protein in the high-affinity site. Considering the sequential mode of binding of Ni(II) to apo-*Sp*UreE, established by ITC, we used the same model to fit the data in the competition experiment. This model produced a statistically consistent fit: $\chi^2_v = 3.4 \times 10^3$, $K_{b1} = 2.4 \pm 0.3 \times 10^5$ M^{-1} ($K_{d1} = 4.2 \pm 0.5$ μM), $\Delta H_1 = -2.9 \pm 0.1$ kcal mol^{-1}, $\Delta S_1 = 15.0$ cal mol^{-1} K^{-1}, $K_{b2} = 1.1 \pm 0.3 \times 10^3$ M^{-1} ($K_{d2} = 0.9 \pm 0.2$ mM), $\Delta H_2 = -15.8 \pm 0.4$ kcal mol^{-1}, and $\Delta S_2 = -39.3$ cal mol^{-1} K^{-1}. This fit features a first event with a binding constant similar to that for the low-affinity event observed on titrating Ni(II) into apo-*Sp*UreE, suggesting that, in the presence of Zn(II) in the high-affinity site, Ni(II) binds to the low-affinity site. The second Ni(II) binding event has a significantly lower binding constant as compared with the apoprotein, and a

Author's personal copy

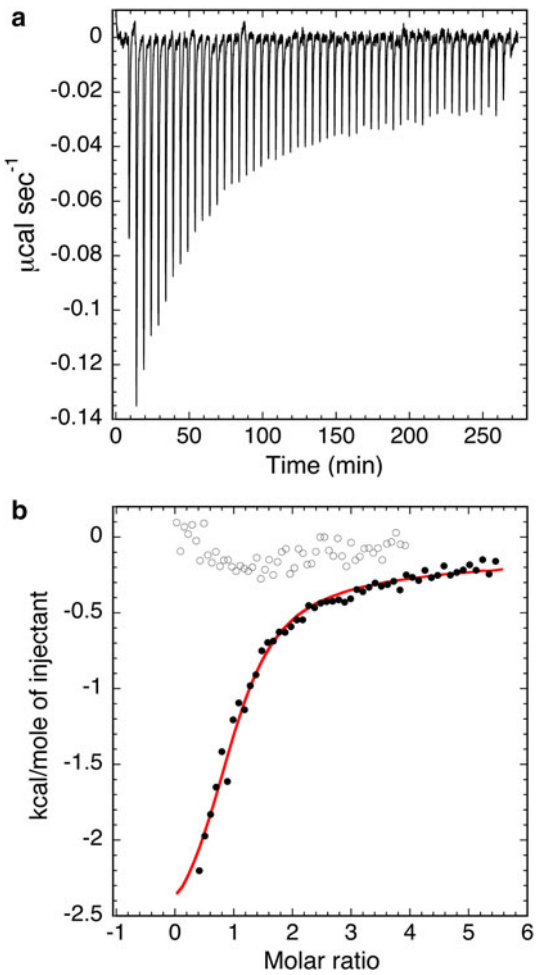

Fig. 11 Ni(II) titration into Zn(II)-bound *Sp*UreE determined using isothermal titration calorimetry. **a** Representative plot of raw direct titration data for Ni(II) (0.5 mM) titrated into *Sp*UreE (19 μM) incubated with 1 equiv of Zn(II). **b** Integrated heat data as a function of metal-to-protein molar ratio. *Filled circles* represent the integrated titration data for Ni(II) titrated into Zn(II)-bound *Sp*UreE. The *continuous line* represents the best fit obtained using a model involving sequential binding of two Ni(II) ions. The *hollow circles* represent the integrated data for Zn(II) titrated into Ni(II)-bound *Sp*UreE, the raw data for which are shown in Fig. S3

consequent absence of positive cooperativity, further supporting the hypothesis that Zn(II) binds to the physiological high-affinity site, but it is outcompeted by Ni(II).

Conclusions

In the urease system, the molecular rationale of delivery of Ni(II) into its final position in the active site of the enzyme should necessarily involve the understanding of the structural basis of Ni(II) selectivity in the nickel chaperone UreE, and the possible interplay of Ni(II) and other metal ions in the physiological conserved site in the center of the protein dimer. In particular, Ni(II) and Zn(II) have been found to be involved in a finely tuned metal ion cross talk: indeed, among the different noncognate metal ions that UreE proteins can bind in vitro [Zn(II), Co(II), Cu(II)] [36, 40], Zn(II) appears to have a role in the *H. pylori* urease maturation process, as it enhances the dimerization of UreG [41] and stabilizes the UreE–UreG interaction [17]. In a previously determined structure of *Sp*UreE [21], Zn(II) was found in the same binding position at the interface of the protein dimer that, in solution, is thought to be occupied by Ni(II). In the present study, the structural basis of metal ion selection and the preference for Ni(II) over Zn(II) in *Sp*UreE were investigated, using an approach that coupled structural determination in the crystalline state by crystallography and characterization of metal binding and competition in solution by calorimetry. The data obtained are consistent with the presence of a high-affinity Ni(II) binding site at the dimer interface involving the two conserved His^{100} residues and the C-terminal His^{145} residues, in addition to a low-affinity site comprising His^{145} and His^{147}, found in the C-terminal disordered arms and acting as nickel storage, able to funnel the Ni(II) ions into the physiological site for metal transport. The calorimetric data, showing a strong positive cooperativity between the two metal binding events, allowed us to discriminate between the two models in Fig. 2, previously proposed on the basis of X-ray absorption spectroscopy experiments [26]. The X-ray diffraction data for the protein bound to both Ni(II) and Zn(II) reveal that this metal binding site is specific for Ni(II) over Zn(II), most likely because of the electronic properties of the two metal ions that dictate different coordination environments. The selectivity of this metal binding site for Ni(II) over Zn(II) has been confirmed in solution by competition experiments using calorimetry. The selective affinity of the UreE dimer for Ni(II) is consistent with its proposed role in transporting Ni(II) cations. The additional metal binding site detected in this study by crystallography, which can host either Ni(II) or Zn(II), could be an artifact, but it could also suggest the presence of a metal binding site involved in the interaction between UreE and UreG, known to be stabilized by Zn(II) [17].

Acknowledgments BZ and AM expressed and purified *Sp*UreE and carried out the calorimetric experiments and data fitting. KB carried out protein crystallization, X-ray diffraction data collection and processing, protein structure solution, refinement and analysis. AK participated in the X-ray experiment and data processing. WR and SC designed the study and interpreted the data. All authors contributed to writing and editing the paper, and approved the final version of the paper. We acknowledge the Helmholtz-Zentrum Berlin for provision of synchrotron radiation at beamlines 14.1 and 14.2 (BESSY II). This work was supported by the European Community's Seventh Framework Programme (2007–2013) (grant 226716 to WR) and by the Italian Ministero dell'Istruzione, dell'Università e della Ricerca PRIN2011 (SC). AM received a PhD fellowship from the University of Bologna.

Author's personal copy

References

1. Carter EL, Flugga N, Boer JL, Mulrooney SB, Hausinger RP (2009) Metallomics 1:207–221
2. Zambelli B, Musiani F, Benini S, Ciurli S (2011) Acc Chem Res 44:520–530
3. Callahan BP, Yuan Y, Wolfenden R (2005) J Am Chem Soc 127:10828–10829
4. Jabri E, Carr MB, Hausinger RP, Karplus PA (1995) Science 268:998–1004
5. Benini S, Rypniewski WR, Wilson KS, Miletti S, Ciurli S, Mangani S (1999) Structure 7:205–216
6. Ha N-C, Oh S-T, Sung JY, Cha KA, Lee MH, Oh B-H (2001) Nat Struct Biol 8:505–509
7. Balasubramanian A, Ponnuraj K (2010) J Mol Biol 400:274–283
8. Balasubramanian A, Durairajpandian V, Elumalai S, Mathivanan N, Munirajan AK, Ponnuraj K (2013) Int J Biol Macromol 58C:301–309
9. Farrugia MA, Macomber L, Hausinger RP (2013) J Biol Chem 288:13178–13185
10. Mobley HLT, Hausinger RP (1989) Microbiol Rev 53:85–108
11. Mobley HLT, Island MD, Hausinger RP (1995) Microbiol Rev 59:451–480
12. Biagi F, Musiani F, Ciurli S (2013) J Biol Inorg Chem 18:571–577
13. Lee MH, Mulrooney SB, Renner MJ, Markowicz Y, Hausinger RP (1992) J Bacteriol 174:4324–4330
14. Park IS, Hausinger RP (1995) Science 267:1156–1158
15. Park I-S, Hausinger RP (1996) Biochemistry 35:5345–5352
16. Soriano A, Colpas GJ, Hausinger RP (2000) Biochemistry 39:12435–12440
17. Bellucci M, Zambelli B, Musiani F, Turano P, Ciurli S (2009) Biochem J 422:91–100
18. Boer JL, Quiroz-Valenzuela S, Anderson KL, Hausinger RP (2010) Biochemistry 49:5859–5869
19. Song H-K, Mulrooney SB, Huber R, Hausinger RP (2001) J Biol Chem 276:49359–49364
20. Yoon JH, Lee KC, Weiss N, Kho YH, Kang KH, Park YH (2001) Int J Syst Evol Microbiol 51:1079–1086
21. Remaut H, Safarov N, Ciurli S, Van Beeumen J (2001) J Biol Chem 276:49365–49370
22. Shi R, Munger C, Asinas A, Benoit SL, Miller E, Matte A, Maier RJ, Cygler M (2010) Biochemistry 49:7080–7088
23. Banaszak K, Martin-Diaconescu V, Bellucci M, Zambelli B, Rypniewski WR, Maroney MJ, Ciurli S (2012) Biochem J 441:1017–1026
24. Benoit S, Maier RJ (2003) J Bacteriol 185:4787–4795
25. Lee MY, Pankratz HS, Wang S, Scott RA, Finnegan MG, Johnson MK, Ippolito JA, Christianson DW, Hausinger RP (1993) Protein Sci 2:1042–1052
26. Stola M, Musiani F, Mangani S, Turano P, Safarov N, Zambelli B, Ciurli S (2006) Biochemistry 45:6495–6509
27. Musiani F, Zambelli B, Stola M, Ciurli S (2004) J Inorg Biochem 98:803–813
28. Higgins KA, Carr CE, Maroney MJ (2012) Biochemistry 51:7816–7832
29. Sivashanmugam A, Murray V, Cui C, Zhang Y, Wang J, Li Q (2009) Protein Sci 18:936–948
30. Pardee AB, Jacob F, Monod J (1959) J Mol Biol 1:165–178
31. Kabsch W (2010) Acta Crystallogr D Biol Crystallogr 66:125–132
32. McCoy AJ, Grosse-Kunstleve RW, Adams PD, Winn MD, Storoni LC, Read RJ (2007) J Appl Crystallogr 40:658–674
33. Murshudov GN, Vagin AA, Dodson EJ (1997) Acta Crystallogr D Biol Crystallogr 53:240–255
34. Emsley P, Cowtan K (2004) Acta Crystallogr D Biol Crystallogr 60:2126–2132
35. Won HS, Lee YH, Kim JH, Shin IS, Lee MH, Lee BJ (2004) J Biol Chem 279:17466–17472
36. Grossoehme NE, Mulrooney SB, Hausinger RP, Wilcox DE (2007) Biochemistry 46:10506–10516
37. Ciurli S, Safarov N, Miletti S, Dikiy A, Christensen SK, Kornetzky K, Bryant DA, Vandenberghe I, Devreese B, Samyn B, Remaut H, van Beeumen J (2002) J Biol Inorg Chem 7:623–631
38. Velazquez-Campoy A, Freire E (2006) Nat Protoc 1:186–191
39. Brown A (2009) Int J Mol Sci 10:3457–3477
40. Ciurli S, Benini S, Rypniewski WR, Wilson KS, Miletti S, Mangani S (1999) Coord Chem Rev 190–192:331–355
41. Zambelli B, Turano P, Musiani F, Neyroz P, Ciurli S (2009) Proteins 74:222–239